1-1-2009

Probing the 2D kinematic structure of early-type galaxies out to 3 effective radii

R. N. Proctor
Swinburne University

D. A. Forbes
Swinburne University

J. P. Brodie
UCO/Lick Observatory

Aaron J. Romanowsky
San Jose State University, aaron.romanowsky@sjsu.edu

J. Strader
Harvard-Smithsonian Centre for Astrophysics

See next page for additional authors

Recommended Citation

R. N. Proctor, D. A. Forbes, J. P. Brodie, Aaron J. Romanowsky, J. Strader, M. Spolaor, J. T. Mendel, and L. Spitler. "Probing the 2D kinematic structure of early-type galaxies out to 3 effective radii" *Monthly Notices of the Royal Astronomical Society* (2009): 91-108. https://doi.org/10.1111/j.1365-2966.2009.15137.x

Mon. Not. R. Astron. Soc. **398,** 91–108 (2009) doi:10.1111/j.1365-2966.2009.15137.x

Probing the 2D kinematic structure of early-type galaxies out to three effective radii

Robert N. Proctor,[1,2⋆] Duncan A. Forbes,[1⋆] Aaron J. Romanowsky,[3] Jean P. Brodie,[3] Jay Strader,[4]† Max Spolaor,[1] J. Trevor Mendel[1] and Lee Spitler[1]

[1]*Centre for Astrophysics & Supercomputing, Swinburne University, Hawthorn, VIC 3122, Australia*
[2]*Universidade de São Paulo, IAG, Rua do Mato 1226, São Paulo 05508-900, Brazil*
[3]*UCO/Lick Observatory, University of California, Santa Cruz, CA 95064, USA*
[4]*Harvard-Smithsonian Centre for Astrophysics, 60 Garden St., Cambridge, MA 02138, USA*

Accepted 2009 May 22. Received 2009 April 2; in original form 2008 October 26

ABSTRACT

We detail an innovative new technique for measuring the two-dimensional (2D) velocity moments (rotation velocity, velocity dispersion and Gauss–Hermite coefficients h_3 and h_4) of the stellar populations of galaxy haloes using spectra from Keck DEIMOS (Deep Imaging Multi-Object Spectrograph) multi-object spectroscopic observations. The data are used to reconstruct 2D rotation velocity maps.

Here we present data for five nearby early-type galaxies to ∼three effective radii. We provide significant insights into the global kinematic structure of these galaxies, and challenge the accepted morphological classification in several cases. We show that between one and three effective radii the velocity dispersion declines very slowly, if at all, in all five galaxies. For the two galaxies with velocity dispersion profiles available from planetary nebulae data we find very good agreement with our stellar profiles. We find a variety of rotation profiles beyond one effective radius, i.e. rotation speed remaining constant, decreasing *and* increasing with radius. These results are of particular importance to studies which attempt to classify galaxies by their kinematic structure within one effective radius, such as the recent definition of fast- and slow-rotator classes by the Spectrographic Areal Unit for Research on Optical Nebulae project. Our data suggest that the rotator class may change when larger galactocentric radii are probed. This has important implications for dynamical modelling of early-type galaxies. The data from this study are available on-line.

Key words: stellar dynamics – techniques: spectroscopic – galaxies: general – galaxies: kinematics and dynamics – galaxies: structure.

1 INTRODUCTION

Since the pioneering work of Simkin (1974), major advances in the measurement of stellar orbits in early-type galaxies have been made. The first quantities to be measured were the line-of-sight rotation velocity ($V_{\rm rot}$; which can be considered a measure of ordered motion within a galaxy) and velocity dispersion (σ; a measure of the random motions). By combining these two measures with photometric ellipticity (ϵ) it was possible to probe the anisotropy of stellar orbits in galaxies (Binney 1978).

Further progress was made in this field when, in the 1980s, Bender (1988) showed that although the isophotal shapes of early-type galaxies were well described by ellipses, small variations from ellipticity could be used to categorize them as either 'boxy' or 'discy', and that these variations relate directly to the stellar orbital isotropy. The combination of surface photometry and detailed kinematics was therefore demonstrated to provide significant insights into the global structure of galaxies.

More recently, higher order moments of the line-of-sight velocity distribution (LOSVD) have been measured (e.g. Bender 1990; Rix & White 1992; Gerhard 1993; van der Marel & Franx 1993). These characterize deviations from a pure Gaussian shape, e.g. skewed and symmetric deviations, denoted h_3 and h_4, respectively. Such parameters can indicate kinematic substructures, such as embedded stellar discs.

⋆E-mail: rproctor@astro.iag.usp.br (RNP); dforbes@astro.swin.edu.au (DAF)
†Hubble fellow.

The development of integral field units (IFUs), such as the Spectrographic Areal Unit for Research on Optical Nebulae (SAURON) instrument, has given new impetus to this field, as these provide two-dimensional (2D) maps of the LOSVD. This allows the definition and estimation of a number of important new parameters that can be averaged over the surface of a galaxy in a self-consistent way. Perhaps the most important of these is the 'spin' parameter (λ_R) which is a proxy for the projected angular momentum per unit mass. Applied to the SAURON galaxy sample of 48 early-type galaxies, it was used to show that a dichotomy exists between 'slow-' and 'fast rotators' (Emsellem et al. 2007). Trends between photometric and kinematic axis ratios and position angles (PAs) have also been shown to vary with λ_R; with slow rotators often exhibiting strong misalignments. These observations provide new clues to the formation mechanisms of these differing galaxy types (Cappellari et al. 2007; Thomas et al. 2007; Krajnović et al. 2008).

Statler & Smecker-Hane (1999) used a different approach to building 2D maps of the LOSVD in NGC 3379. Using long-slit spectroscopy along four PAs, they were able to reconstruct a model of the 2D kinematics by making suitable interpolations between their observed axes. However, such studies are rare due to the large amount of telescope time required to observe multiple PAs out to large radii.

Despite these advances, most observations typically reach to less than one effective radius ($R_{\rm eff}$), with only a handful of studies extending this coverage up to 2–3 $R_{\rm eff}$ (but see Saglia et al. 1993; Graham et al. 1998; Mehlert et al. 2000; Proctor et al. 2005; Sánchez-Blázquez, Gorgas & Cardiel 2006; Forestell & Gebhardt 2008). However, such outer regions potentially provide key information regarding the physical properties of galaxies. For example, radii within 1 $R_{\rm eff}$ only sample 50 per cent of the baryonic mass and ∼10 per cent of the angular momentum of an idealized galaxy with an $R^{1/4}$ like light profile and a flat rotation profile. The situation is even worse when considering the distribution of total galaxy mass (including dark matter). For instance, the simulations of Dekel et al. (2005) show that only ∼5 per cent of the total mass is contained within 1 $R_{\rm eff}$ (see also Mamon & Lokas 2005). Furthermore, the signatures of some formation mechanisms only become apparent at large galactocentric radii (e.g. Weil & Hernquist 1996; McMillan, Athanassoula & Dehnen 2007). A means to probe the kinematics in the outer regions of early-type galaxies, and hence include a significant fraction of a galaxies' angular momentum and mass, is therefore highly desirable.

In this paper we measure stellar LOSVDs from deep multi-object spectroscopic observations and develop a new technique for their analysis. Specifically, we measure rotation velocity, velocity dispersion and the Gauss–Hermite coefficients h_3 and h_4, out to ∼3 $R_{\rm eff}$ in five nearby early-type galaxies. By extending the region studied to such radii we encompass more than 85 per cent of the baryonic mass, 30 per cent of the angular momentum and 15 per cent of the total mass, a significant increase in the fractions so surveyed in galaxies. To achieve this we exploit the large aperture of the Keck telescope, the high sensitivity of the Deep Imaging Multi-Object Spectrograph (DEIMOS) instrument at 8500 Å and the strong calcium triplet absorption features at these wavelengths. Even with this configuration, exposures of ∼2 h are required for our analysis.

The paper is organized as follows: in Section 2 we outline the observations and data reductions, detailing the technique by which we extract the host galaxy spectra. In Section 3 we outline our new kinematic analysis technique. Results are presented in Section 4. We discuss our findings in Section 5, and present our conclusions in Section 6.

2 OBSERVATIONS AND DATA REDUCTION

2.1 Sample selection

The galaxies in our sample were selected with the intention of obtaining spectra of their globular clusters (GCs). The galaxies are all nearby, early types with moderately rich GC systems. The selection also had the requirement that recession velocities were such that the calcium triplet lines would not generally be adversely affected by strong sky lines. The main science goal was to obtain GC kinematics, and hence probe the mass profile of their host galaxy haloes. Initial results for NGC 1407 from the 2006 November run have recently been reported in Romanowsky et al. (2008).

2.2 Observations

The data used in this work are from three observing runs using DEIMOS on the Keck-2 telescope. The first observing run was carried out in 2006 November using the 1200 l/mm grating centred at ∼7500 Å and a 1-arcsec slit. This allows coverage of the calcium triplet at 8498, 8542 and 8662 Å at a resolution of ∼1.5 Å. The second run was carried out in 2007 November and the third in 2008 April, both using the same instrument set-up as the first run. Seeing was ∼0.5 to 0.8 arcsec on all nights. A total of five galaxies were observed (NGC 821, NGC 1400, NGC 1407, NGC 2768 and NGC 4494).

Between two and six independent masks were observed per galaxy and the 16 × 5 arcmin^2 field-of-view allowed the observation of ∼80–120 spectra in each mask. However, only ∼20 per cent of these were at radii from which the signal of the background host galaxy was sufficient for the extraction of spectra.

Fig. 1 shows the positions of slits from which host galaxy spectra were extracted. We note that it was only possible to measure recession velocities in some of the outermost slits, i.e. velocity dispersion and higher order moments are not presented for some of the outermost positions.

2.3 Data reduction

Data reduction was carried out using the DEIMOS DEEP2 pipeline software. This package produces a variety of outputs from the raw DEIMOS data, including both object and 'sky' spectra. The data reported here probe the kinematics of the stellar populations in the galaxy haloes. These are based on the 'sky' spectra that were subtracted from the GC spectra (the prime targets of the observation; see Romanowsky et al. 2008). The 'sky` spectra actually consist of a co-addition of the true sky and the background galaxy light. In order to distinguish them from the *true* sky spectrum we shall therefore henceforth refer to these as the 'background' spectra.

The recovery of the galaxy spectra requires an estimate of the true sky spectrum in each of the background spectra. For each mask, the sky spectra were estimated from the average of four to six of the background spectra sampling large distances from the galaxy centre (see below). These generally lay beyond ∼6–7 $R_{\rm eff}$. Even at this distance some galaxy light is still present. However, since the data reported here are limited to within ∼3 $R_{\rm eff}$, the galaxy light contamination of the sky estimates constitutes only a small fraction of the galaxy light in our science spectra. Assuming a de Vaucouleur's (1953) $R^{1/4}$ profile, we estimate that, in points at 3 $R_{\rm eff}$, the sky estimate contains only <10 per cent of the galaxy light in the science spectra. This falls to ∼4 per cent at 2 $R_{\rm eff}$. Errors caused

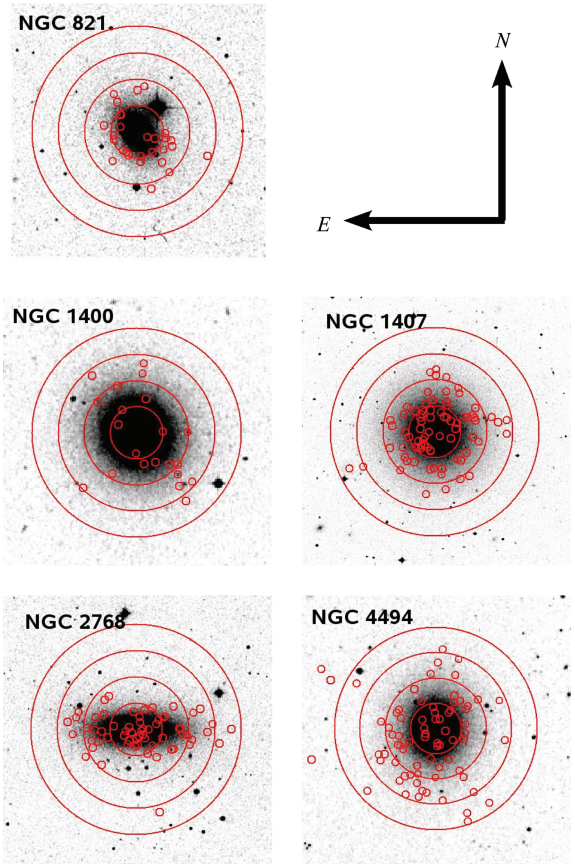

Figure 1. DSS images of the five target galaxies. Small red circles mark the location of slits from which galaxy background spectra were obtained. Large red circles represent 1, 2, 3 and 4 $R_{\rm eff}$.

Table 2. Band definitions for the sky index used in the selection and subtraction of sky spectra.

Band	Wavelengths
Sideband 1	8526.0–8536.0 Å
Central band	8605.0–8695.5 Å
Sideband 2	8813.0–8822.0 Å

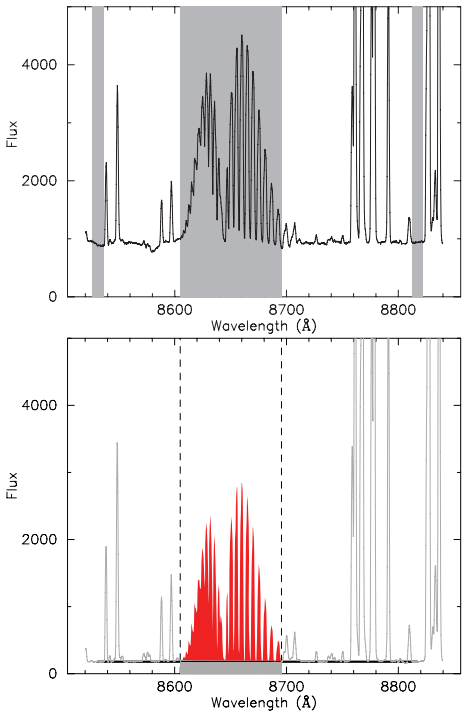

Figure 2. Definition of the sky index. Upper plot shows wavelength regions of the two sidebands and the central band in a spectrum with significant galaxy halo signal. Lower plot shows the region used in the calculation of the sky index in a scaled sky spectrum. The index is defined as a ratio, i.e. excess flux in the central band (counts in shown in red) divided by continuum flux (counts shown in grey).

by the residual galaxy light in our sky estimates are therefore likely to be much smaller than the quoted errors on data points at these radii, which are often as much as ∼30 per cent of the measured parameter values.

In order to select and characterize the sky spectra, a sky index was defined (see Table 2 and Fig. 2). The central band of this index was defined to cover the strong sky emission lines between 8600 and 8700 Å. The sidebands of the index were chosen to cover regions of the background spectra that were relatively free of both significant sky emission lines *and* galaxy absorption features. For each background spectrum the sky index was then calculated as follows: first, the continuum level in the region of the *central* band was estimated by integrating under the linear interpolation of the average fluxes in the sidebands. Then the *excess* flux in the central band was calculated as the total flux in the region minus the

Table 1. Properties of galaxies featured in this work. Distances are from surface brightness fluctuations by Tonry et al. (2001), with the distance moduli modified by −0.16 according to Jensen et al. (2003). The values for NGC 1400 and NGC 1407 are taken as the average of their individual values. Hubble types are from NASA/IPAC Extragalactic Database (NED) and effective radii are from RC3. Absolute K-band magnitudes are calculated from 2MASS apparent magnitudes and the distances given in column 3. Photometric PAs ($\rm PA_{phot}$) and K-band photometric axis ratios are from 2MASS. Systemic velocities are the values derived from our fitting of central data points (see Section 4).

Galaxy	Hubble type	Distance (Mpc)	$R_{\rm eff}$ (arcsec)	M_K (mag)	$\rm PA_{phot}$ (°)	Axis ratio (K band)	$V_{\rm sys}$ (km s^{-1})
NGC 821	E6?	22.4	50	−23.6	30	0.62	1729
NGC 1400	SA0-	25.7	29	−23.8	35	0.90	574
NGC 1407	E0	25.7	70	−24.9	60	0.95	1782
NGC 2768	$\rm S0_{1/2}$	20.8	64	−24.6	93	0.46	1327
NGC 4494	E1–2	15.8	49	−24.8	173	0.87	1335

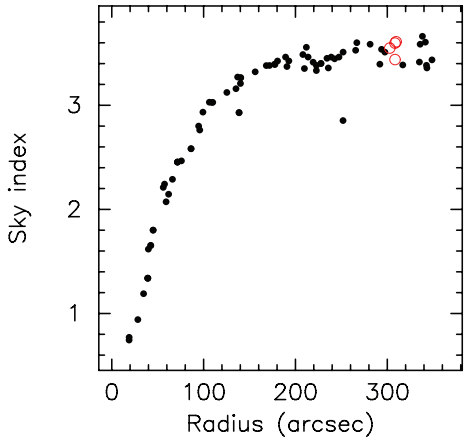

Figure 3. Sky index with radius for one set of NGC 4494 observations. Open red circles represent points whose spectra were co-added to generate the sky spectrum. Two points clearly exhibit aberrant behaviour. These are *not* included in the final sample.

integrated continuum flux. Finally, the sky index was calculated as the ratio of the excess central band flux to its continuum flux (see Fig. 2, bottom). The index has the property that, as one moves away from the galaxy centre (and the galaxy light contribution to the background spectrum decreases), the index tends to a constant value (see Fig. 3). After a careful visual inspection of the spectra, the background spectra to be used as sky estimates were selected from this constant region. These were co-added to provide a higher signal-to-noise ratio estimate of the sky spectrum.

The index was used to select candidate sky spectra, rather than simply choosing the slits at the greatest distance from the galaxy centre, as the index allows identification of spectra suffering from reduction problems not detected by visual inspection. For the most part, these proved to be either slits located near the edges of the mask where vignetting effects are large, or slits in which residual GC light was still present. Fig. 3 illustrates how the sky index allows identification (and elimination) of slits with such problems.

Sky subtraction was carried out by consideration of the *excess flux* in the central band as defined above. First, for each background spectrum, we scaled the sky estimate such that the resultant spectrum had the same excess counts as the target spectrum. Subtraction of the scaled sky spectrum therefore resulted in a spectrum with no excess counts in the sky band region, i.e. with counts in the sky band region equal to the continuum level in the side bands. This method provides a sky subtraction accurate to approximately one count over the sky band region. We show examples of sky subtracted spectra in Fig. 4 in which it can be seen that although sky residuals are present, these are not significantly larger than the Poisson noise associated with the strong sky-lines. Assuming a dark-sky brightness at Mauna Kea of 1–20 mag arcsec^{-2}, then our galaxy halo spectra can reach as low as 1–10 per cent of the sky background. We note that this sky subtraction technique is similar to that used in Norris et al. (2008) and Proctor et al. (2008) in the analysis of optical spectra from GEMINI/GMOS.

3 ANALYSIS METHOD

The analysis presented here involves measurement of velocity moments (V, σ and the Gauss–Hermite coefficients h_3 and h_4) using the pPXF code of Cappellari & Emsellem (2004) – an extension of the pixel fitting code of van der Marel (1994).

3.1 Measurement of kinematics

The pPXF software works in pixel space, finding the combination of template stars which, when convolved with an appropriate LOSVD, best reproduces the galaxy spectrum. 13 template stars were used, ranging in spectral type from F8 to M1. This method of kinematic analysis has the advantage that template-mismatch issues are all but eliminated. Operating in pixel space, the code also permits the masking out of regions of the galaxy spectrum during the measurement. This is of particular importance in our data as, despite the accurate sky subtraction, the spectra still suffer from skyline residuals (see Fig. 4). The code also allows suppression of the higher order moments h_3 and h_4 (i.e. fitting only $V_{\rm obs}$ and σ). This was found to be useful in order to stabilize the fits in low signal-to-noise ratio spectra.

Errors were estimated from a repeat observation on different nights of one of the masks of NGC 2768. By binning the 60 repeat measurements by observed signal (i.e. counts), the rms variations of each of the velocity moments in the repeat measurements were calculated as a function of signal-to-noise ratio. The trend of rms with signal-to-noise ratio so obtained was then used to make estimates of errors in this, and other galaxies.

As a test of the accuracy of our measurements we compared them to those of SAURON (Emsellem et al. 2004) for the two galaxies in common between the studies. This was possible as our data samples 10 precise locations (nine in NGC 2768 and one in NGC 821) that are also sampled by SAURON. The results of the comparison for σ and h_3 are shown in Fig. 5. A small systematic offset of $-12.9\,{\rm km\,s^{-1}}$ is evident in our velocity dispersion data compared to the SAURON values, with a scatter of $7.3\,{\rm km\,s^{-1}}$. The measured h_3 values are consistent within their errors. We do not compare h_4, as errors are generally large with respect to our measured values. We leave comparison of $V_{\rm obs}$ to the sections presenting our results.

During the analysis significant discrepancies were detected between our results for the σ values of NGC 1400 and NGC 1407 and the long-slit data of Spolaor et al. (2008a). As a consequence, the data of Spolaor et al. (2008a) were reprocessed through the

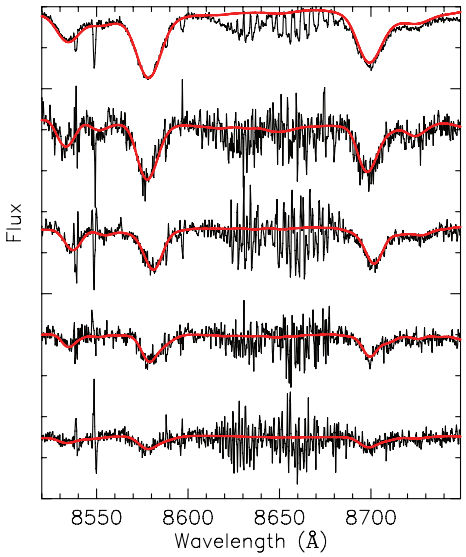

Figure 4. Sky subtracted spectra of NGC 2768. Red lines show the best-fitting template derived by the pPXF code during measurement of velocity moments. Spectra are in order of decreasing signal-to-noise ratio broadly covering the range within our data (from ∼40 in the top spectrum down to seven in the bottom spectrum).

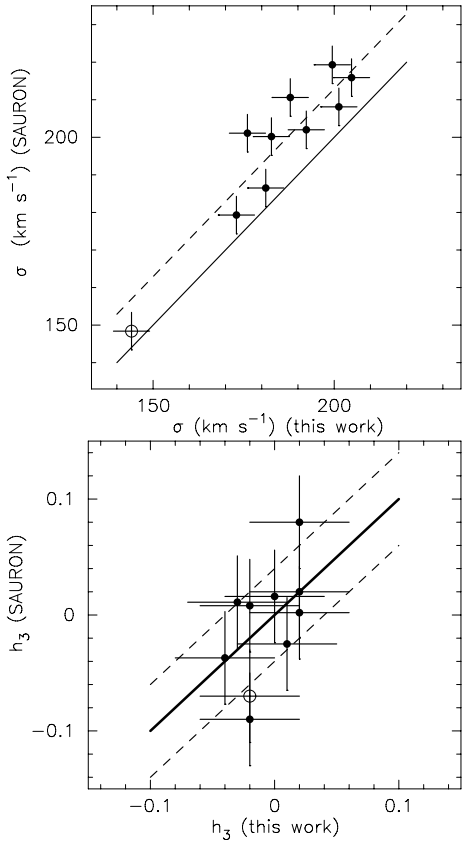

Figure 5. Comparison of velocity dispersion measures (top) and h_3 (bottom) with SAURON data (Emsellem et al. 2004). Filled symbols are from NGC 2768, and the open symbol from NGC 821. In the plot of σ, the one-to-one (solid) and $-12.9\,{\rm km\,s^{-1}}$ offset (dashed) lines are shown. In the plot of h_3 the one-to-one line (solid) and typical errors (dashed) of ±0.04 are shown.

pPXF software using a large number of template stars, resulting in significantly improved measurements (see Appendix A).

The measured velocity moments of all five galaxies are available on-line. An example of the available data is presented in Table 3.

3.2 Kinemetry

Our analysis of these data proceeds by consideration of the velocity moments in the space of galactocentric radius and PA (defined as the angle between the point in the galaxy and the galaxy centre from north through east). For the analysis, the data were binned in radial ranges (i.e. circular shells) for comparison to the expectations for rotating isotropic ellipsoids (or, equivalently, inclined discs). Fits of the observed velocity ($V_{\rm obs}$) data were carried out by least-squares minimization of the data to the equation:

$$V_{\rm obs} = V_{\rm sys} + V_{\rm rot}\cos(\phi), \tag{1}$$

where $V_{\rm sys}$ is the systemic velocity of the system, $V_{\rm rot}$ is the major axis rotation velocity and ϕ is defined as

$$\tan(\phi) = \frac{\tan({\rm PA} - {\rm PA_{kin}})}{q}, \tag{2}$$

with $\rm PA_{kin}$ the PA of the major rotation axis and q the rotation axis ratio. The values of $V_{\rm rot}$, $\rm PA_{kin}$ and q were all allowed to vary freely. Values of $V_{\rm sys}$ were taken as the value derived from the high signal-to-noise ratio data of our innermost points (i.e. generally the points within $1\,R_{\rm eff}$). This value was then assumed for all radial bins.

In the analysis of the rotation properties of our sample galaxies we used two types of radial binning. The first was to break the data into two or three independent radial slices (i.e. into circular annuli), the other was to carry out rolling fits again with data binned in circular annuli. Results are presented as the major axis values with radii expressed in terms of the $R_{\rm eff}$.[1] Errors on these fits were estimated as the rms scatter in the results of 50 Monte Carlo simulations of the data using the best-fitting parameter values and scatter.

We were not however able to carry out such an analysis on the velocity dispersion data, mainly because we detect little to no variation in this parameter over the radii probed by our data. We are therefore not able to measure the axis ratio of this velocity moment. However, for two galaxies (NGC 821 and NGC 2768), the SAURON data of Emsellem et al. (2004) permit estimation of axis ratios of σ in the inner regions. For NGC 821 the SAURON data appear to show an axis ratio close to 1.0 (despite the ellipticity of the galaxy isophotes). On the other hand, in NGC 2768 σ appears to have a similar axis ratio to the isophotes. We therefore adopt these axis ratios for the analysis of the velocity dispersion data from these galaxies. For the remaining three galaxies (all of which have axis ratios $\geq$0.8) we assume an axis ratio of 1.0.

We also experimented with the co-adding of spectra at similar effective radii for σ measurement. However, this process requires the spectra to be deredshifted prior to co-addition, which complicates the handling of the sky-line residuals in the absorption features. In addition the results proved almost identical to the values obtained by averaging individual measurements. On the basis that simplest is best, we therefore present σ values as individual and radially averaged values.

Our analysis is similar in intent to the 'kinemetry' of the SAURON paper by Krajnović et al. (2006). However, our data possess an extremely low sampling density (i.e. we have on average 60 points inside an area of 24 $R_{\rm eff}^2$ compared to SAURON's $\sim$3000 points inside 0.4 $R_{\rm eff}^2$ – a data density contrast of 3000:1). Our data are also generally of lower signal-to-noise ratio than the SAURON data. Since, as noted in Krajnović et al. (2006), such limitations make it impossible to perform a full harmonic analysis, we have restricted our analysis to only the low-order harmonics and fitted our data on circles (or more precisely on annuli) rather than ellipses. Unable to perform the full analysis, we have also refrained from adopting the full notation used by Krajnović et al. (2006). However, we note that the rotation velocity ($V_{\rm rot}$) we report is most directly related to their k_1 parameter, while the kinematic axis ratio is most directly related to their $q_{\rm kin}$ parameter. $\rm PA_{kin}$ has the same meaning in both studies.

4 RESULTS

In this section we present the results of our velocity moment measurements ($V_{\rm obs}$, σ, h_3 and h_4). Errors on individual data points were derived from the repeat measurement of one mask in NGC 2768 (see Section 3). Errors on rolling fits were estimated by Monte Carlo realizations of the best-fitting parameters. Note that, for the lowest signal-to-noise ratio spectra, the higher order moments either were suppressed altogether or are not presented. Tests on the low signal-to-noise ratio spectra show that changes in recession

[1] Note that $R_{\rm eff}$ is expressed as the radius of a circle with the same area as the ellipse encompassing 50 per cent of the galaxy light. Therefore, in galaxies with non-zero ellipticity, a point on the major axis at $1\,R_{\rm eff}$ does *not* lie on, but rather within, the half-light ellipse.

Table 3. Example of the velocity moment data form this work. Columns are RA and Dec. (J2000), observed recession velocity ($V_{\rm obs}$ in km s^{-1}), velocity dispersion (σ in km s^{-1}) and Gauss–Hermite coefficients h_3 and h_4. The full table is available in the online version of the paper (see Supporting Information).

RA	Dec.	$V_{\rm obs}$	$V_{\rm obs}$ error	σ	σ error	h_3	h_3 error	h_4	h_4 error
NGC 2768									
9:11:31.97	+60:1:38.7	1300	26	152	24	0.14	0.04	0.10	0.05
9:11:28.47	+60:2:51.5	1251	27	177	25	0.05	0.04	0.03	0.05
9:11:35.29	+60:2:03.8	1284	5	192	4	0.02	0.04	0.02	0.05
9:11:38.70	+60:2:57.4	1346	26	154	24	−0.02	0.04	−0.01	0.05
...	...	...	...	...	...	...	...	...	...

velocity and velocity dispersion caused by the suppression of the h_3 and h_4 parameters are ∼20 per cent of the quoted errors. We also present reconstructions of 2D rotation velocity maps in this section.

The results of the fits to independent radial slices are presented in Table 4. In NGC 821 and NGC 1400 two radial ranges were defined (NGC 821: $R < 1.0\,R_{\rm eff}$ and $R \geq 1.0\,R_{\rm eff}$; NGC 1400: $R < 1.5\,R_{\rm eff}$ and $R \geq 1.5\,R_{\rm eff}$). In the other three galaxies three ranges were defined ($R < 1.0\,R_{\rm eff}$, $1.0\,R_{\rm eff} \leq R < 2.0\,R_{\rm eff}$ and $R \geq 2.0\,R_{\rm eff}$).

We first present our results for NGC 2768, as this galaxy possesses high signal-to-noise ratio data, a large sample size, and is also one of the galaxies observed by SAURON.

4.1 NGC 2768

The brightest galaxy in a loose group, NGC 2768, is classified as an E6 galaxy in de Vaucouleurs et al. (1991, hereafter RC3). However, in both the Revised Shapley–Ames Catalogue of Bright Galaxies (Sandage, Tammann & van den Bergh 1981) and the Carnegie Atlas of Galaxies (Sandage & Bedke 1994) it is classified as an $S0_{1/2}$ due to a 'definite outer envelope'. The galaxy is highly elliptical with K-band photometric axis ratio of 0.46, and PA of 93° (Jarrett et al. 2000). It also reveals a polar orbiting dust and gas ring, possibly of external accretion origin (see Martel et al. 2004 and references therein).

Photometric profiles out to 200 arcsec are presented in Peletier et al. (1990). They find a rapidly rising ellipticity profile with radius (i.e. a falling axis ratio), and report indications of a 'disc-like component' at about 50 arcsec which gives way to boxy isophotes beyond about 100 arcsec.

Fried & Illingworth (1994) probed the kinematics along the minor and major axes out to about 50 arcsec. They found evidence for stellar rotation aligned along the photometric major axis and an 'spheroidal' velocity field. They also detected minor axis rotation associated with the polar ring.

The central regions (∼80 × 40 arcsec^2) of the galaxy were also observed with the SAURON IFU (Emsellem et al. 2004). The SAURON results show strong rotation with a 'cylindrical velocity field' and a central dip in σ (McDermid et al. 2006). They find the galaxy to be a fast rotator, but, contrary to Sandage & Bedke (1994), conclude that the galaxy '... does not have evidence for a disc'. They therefore adopt the RC3 classification of this galaxy as an E6.

The SAURON team also investigated the very central regions (∼4 × 4 arcsec^2) using the Optically Adaptive System for Imaging Spectroscopy (OASIS) integral field spectrograph (McDermid et al. 2006), identifying emission associated with the polar disc and a young (2.5 Gyr) central stellar population. However, other spectroscopic age determinations in the literature generally prove inconsistent, with studies reporting the central stellar population to be both old and young (e.g. Denicoló et al. 2005; Howell 2005; Sil'Chenko 2006). It is unclear whether this reflects inconsistencies in the determination of the properties of the central populations, or is rather a real effect, perhaps caused by variable sampling of the central star-forming disc.

Table 4. Kinematic data summary for independent radial slices. The definition of the radial binning is outlined in Section 4. The number of slits in each radial bin, their average radius and σ are given as well as the results of the rotation velocity fits (equations 1 and 2). Data in brackets are assumed (rather than fitted) values.

Galaxy	No	$\langle R \rangle$ (arcsec)	$\langle R/R_{\rm eff} \rangle$ ($R_{\rm eff}$)	$\langle \sigma \rangle$ (km s^{-1})	$V_{\rm rot}$ (km s^{-1})	Axis ratio (q)	PA$_{\rm kin}$ (°)
NGC 2768	21	31	0.48	174 ± 4	98 ± 3	0.45 ± 0.06	90±3
	26	93	1.45	152 ± 4	178 ± 6	0.30 ± 0.08	94±2
	15	165	2.57	123 ± 10	190 ± 16	0.35 ± 0.13	88±6
NGC 4494	19	32	0.65	133 ± 3	58 ± 2	0.80 ± 0.03	182 ± 1
	30	75	1.53	111 ± 3	52 ± 3	0.50 ± 0.09	179 ± 3
	33	143	2.91	100 ± 5	54 ± 5	0.40 ± 0.20	170 ± 6
NGC 1407	28	49	0.70	261 ± 6	28 ± 4	(0.95)	254 ± 8
	39	102	1.46	240 ± 7	21 ± 6	(0.95)	245 ± 14
	14	173	2.48	198 ± 11	20 ± 10	(0.95)	248 ± 15
NGC 1400	7	31	1.07	116 ± 3	53 ± 3	(0.9)	34 ± 4
	14	68	2.35	96 ± 7	30 ± 7	(0.9)	40 ± 14
NGC 821	14	41	0.82	149 ± 5	56 ± 8	0.30	33
	17	78	1.56	144 ± 6	6 ± 8	(0.30)	(33)

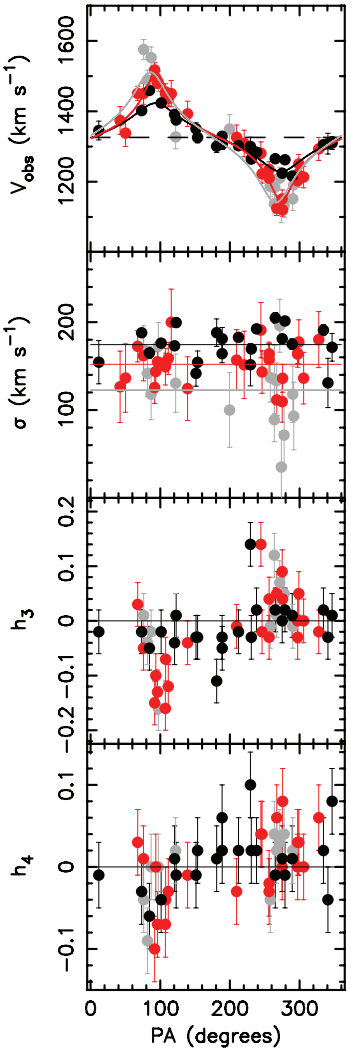

Figure 6. *NGC 2768*. Velocity moments are plotted against PA. Data points are coloured according to galactocentric radius (black, $R < 1\,R_{\rm eff}$; red, $1\,R_{\rm eff} < R < 2\,R_{\rm eff}$; grey, $R > 2\,R_{\rm eff}$). In the plot of $V_{\rm obs}$ best-fitting elliptical models at each radius are shown as appropriately coloured lines. The systemic velocity ($V_{\rm sys}$) is shown as a dashed line. The major kinematic axis ($\rm PA_{kin}$) is at ∼90°. In the plot of σ average values are also shown as appropriately coloured lines. The values adopted for these lines are presented in Table 4.

Hakobyan et al. (2008) suggest this galaxy may be a merger remnant with the presence of a young stellar population suggested by '*. . . the existence of strong HI and CO emission, and the presence of dust and ionized gas. . .*'. The recent Type Ib supernova SN2000ds (Filippenko & Chornock 2000) supports this conclusion.

Presenting our results, we first consider the distribution of the NGC 2768 velocity moments with PA. Results are plotted in Fig. 6 with point colour depicting galactocentric radius. Values derived for each radial bin are presented in Table 4.

The rotation in this galaxy can be seen to be strongly elliptical. An increasing rotation velocity with radius is also evident. The h_3 parameter reflects this behaviour, with near-zero values in the slowly rotating inner regions ($R < 1\,R_{\rm eff}$). However, at larger radii h_3 increasingly mirrors the elliptical rotation curve. The increasing signal in h_3 with radius is also detected in the SAURON maps of the galaxy (Emsellem et al. 2004).

Both σ and h_4, however, exhibit unusual behaviour, as they do not possess the minor-axis symmetry expected from even moments (see Krajnović et al. 2008). This must be understood in terms of the degeneracy between σ and h_4 discussed at length in Cappellari & Emsellem (2004). The degeneracy is worst when (i) signal-to-noise ratio is low, and (ii) two distinct kinematic components have roughly equal luminosities. To test that this was indeed causing the lack of axisymmetry in our data, we refitted the data for this galaxy using pPXF with h_3 and h_4 suppressed (i.e. set to zero). The test confirmed that, if h_4 is forced to zero, the dip in σ becomes visible on both sides of the galaxy.

Given that the h_4 parameter is more prone to the effects of low signal-to-noise ratio and sky-line residuals than σ, we conclude that, in its outer reaches, this galaxy probably exhibits a significant drop in σ on both sides of the major axis, as would be expected from the disc of an S0 galaxy.

Velocity dispersion appears to be decreasing with increasing radius (Fig. 6 and Table 4). However, the dip on the major axis (PA ∼ 270°) is clearly effecting measured average values, particularly since the slits in the outer regions of the galaxy from which we were able to recover a galaxy spectrum tend to lie along the major axis where the galaxy light is brightest (Fig. 6). The gradient in σ presented here may therefore be somewhat exaggerated by this effect. We note for future reference that the four data points with $\sigma < 100\,{\rm km\,s^{-1}}$ all lie very close to the major rotation velocity axis.

To measure variations with radius we carried out a rolling fit to the recession velocity data in annuli at increasing radii allowing $V_{\rm rot}$, $\rm PA_{kin}$ and kinematic axis ratio (q in equation 2) to vary with radius. The fits were performed using a minimum of 10 data points, increasing to 20 in the outer regions. Results of these fits are presented in Fig. 7. We also performed rolling fits to the SAURON data (Emsellem et al. 2004) for comparison.

The agreement in $V_{\rm rot}$ between our results and the SAURON data is good, with near identical rotation velocities over the whole ∼20 arcsec overlap region. However, the rotation velocity clearly continues to rise beyond the extent of the SAURON data, with the rotation velocity doubling to $\sim 200\,{\rm km\,s^{-1}}$ between 1 and $3\,R_{\rm eff}$. This has a significant impact on the value of V/σ obtained for this galaxy, underlining the importance of data at large radii in the construction of even simple kinematic descriptions of galaxies (see Section 5).

Also shown in Fig. 7 is a plot of σ with radius. In this plot the agreement between the SAURON results (Emsellem et al. 2004) and ours can be seen to be reasonable. However, the comparison of σ presented in Fig. 5 is largely based on data from this galaxy, and exhibits a $\sim 13\,{\rm km\,s^{-1}}$ systematic offset. The results indicate a strong radial trend in σ within $1\,R_{\rm eff}$, which levels off somewhat beyond. However, we again note the increasing tendency for our outer data points to lie along the major kinematic axis and the trend for such points to possess depressed σ. To get some idea of the impact these trends might have on our results, consider the four points with the lowest σ ($<100\,{\rm km\,s^{-1}}$), which, as noted in the previous section, all lie very close to the major kinematic axis. If these points are excluded from our considerations we would conclude that σ was flat beyond $\sim 1\,R_{\rm eff}$.

We detect a $\rm PA_{kin}$ of 91° ± 3° throughout the galaxy in good agreement with the photometric PA from Two Micron All Sky Survey (2MASS; Jarrett et al. 2000) and Peletier et al. (1990). We detect no variation in $\rm PA_{kin}$ with radius, with our measurements of the SAURON data yielding the same, near-constant value.

Comparison of our rotation axis ratio measurements to those of SAURON again gives good agreement in the overlap region. The

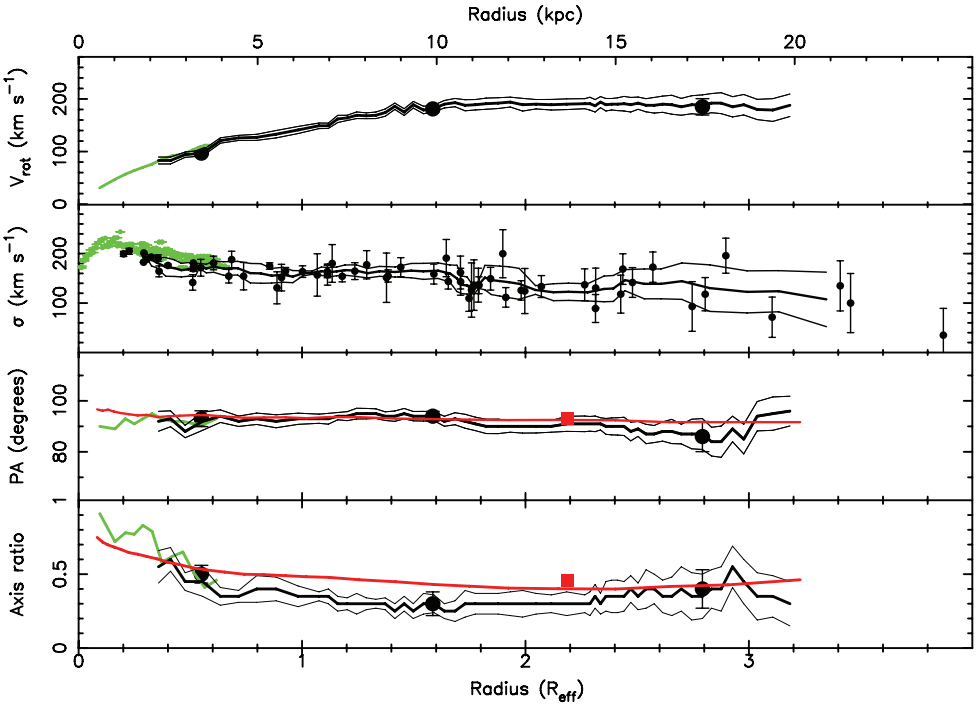

Figure 7. *NGC 2768*. Radial profiles of the major axis rotation velocity (V_{rot}), σ, kinematic and photometric PA (PA_{kin} and PA_{phot}) and axis ratio (q and 1ϵ). Note that ellipticity of σ is assumed to be 0.54, i.e. the photometric ellipticity. The physical radial distances (based on data in Table 1) are given in kiloparsec on the top axis. The σ data points (black) are the individual measured values, with the line representing a rolling average of five points. For all other parameters the black data points represent the values of our fits to independent regions (Table 4). The results of rolling fits to the data and their 1σ errors are indicated as black lines. Green data points and lines at small radii are from our analysis of the SAURON data of Emsellem et al. (2004). The red squares in PA and axis ratio are the 2MASS photometric values at the radius of the *K*-band 20th mag isophote, while the red lines show the *R*-band photometric data of Peletier et al. (1990). Overall the agreement with the literature values is very good.

results clearly indicate that the rotation in the central regions, variously described as 'cylindrical' (Emsellem et al. 2004) or 'spherical' (Fried & Illingworth 1994), rapidly give way to much more disc-like values at larger radii. Interestingly, the comparison with the photometric axis ratios of 2MASS and Peletier et al. (1990) shows the rotation axis ratio to pass from less than the photometric axis ratio in the outer regions to greater than the photometric axis ratio in the inner regions. The most natural explanation for the galaxy having a smaller photometric than kinematic axis ratio in the inner regions is the presence of a highly inclined, but inflated disc, such as would be found in an S0 galaxy, in accord with the Sandage et al. (1981) and Sandage & Bedke (1994) classifications.

To aid in the visualization of our results, and to facilitate the comparison of our results with those of SAURON, we have reconstructed the 2D velocity map of NGC 2768 in Fig. 8. The image was generated using the rolling fit values of V_{rot}, PA_{kin} and rotation axis ratio of Fig. 7. Agreement with the SAURON results can be seen to be extremely good. Also evident is the progression from 'cylindrical' rotation in the inner, bulge-dominated regions to discy rotation in the outer regions probed by our data.

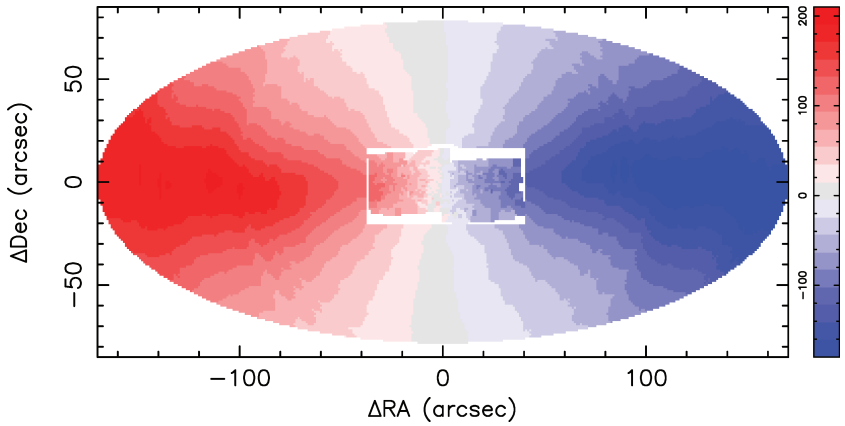

Figure 8. *NGC 2768*. Reconstruction of the 2D rotation velocity map using the rolling fits of Fig. 7. The outer boundary of the map has been chosen to reflect the photometric axis ratio of the galaxy (0.46). The colour scale (in km s^{-1}) is shown on the right. Also shown is the SAURON (Emsellem et al. 2004) velocity map of the central regions of the galaxy. The agreement between the data sets is extremely good.

In summary, our results for this galaxy are all in accord with the Shapley–Ames Catalogue (Sandage et al. 1981) and Carnegie Atlas of Galaxies (Sandage & Bedke 1994) classifications of this galaxy as an S0, with the disc-like kinematics in the outer regions giving way to the more 'cylindrical' rotation in the inner regions.

4.2 NGC 4494

NGC 4494 is an elliptical galaxy in the Coma I cloud (Forbes et al. 1996) with a *K*-band photometric PA of 173° and axis ratio of 0.87 (Jarrett et al. 2000). It reveals a small central dust ring with ∼60° inclination (photometric axis ratio ∼0.5) aligned with the major axis of the galaxy (Carollo et al. 1997). The central regions also host a kinematically distinct core (Bender 1988). The mass modelling analysis of Kronawitter et al. (2000) indicates a rising *M*/*L* profile. However, evidence for dark matter in NGC 4494 has been questioned by Romanowsky et al. (2003) based on an extended σ profile from planetary nebulae (PNe) kinematics (but see also Dekel et al. 2005; Napolitano et al. 2009). The stellar population analysis of Denicoló et al. (2005) found an intermediate age of 6.7 Gyr in the central regions, indicating that this is not a simple, old, passively evolving elliptical galaxy.

Our analysis of this galaxy was the same as that for NGC 2768. The distribution of the velocity moments with PA is shown in Fig. 9. Results show the rotation in this galaxy to be strongly elliptical, but rotation velocity shows no sign of variation with radius. Within 1 $R_{\rm eff}$, the h_3 parameter shows the anticorrelation with $V_{\rm rot}$ expected from a disc embedded in a more slowly rotating (or non-rotating) bulge, although it is not possible to trace this behaviour out to the outer regions where the signal-to-noise ratio is low. We find a decreasing σ with radius which flattens out beyond 1 $R_{\rm eff}$. We find no evidence for variation of σ with PA.

The rolling fits to $V_{\rm obs}$ are presented in Fig 10. These fits were performed using 10 data points in the inner region rising to 20 data points in the outer regions of the galaxy. For $V_{\rm rot}$, we find good agreement with profiles in the literature. Our results are also consistent with the PNe data of Napolitano et al. (2009) in the outer regions (notwithstanding their large uncertainties). As deduced from Fig. 9, the galaxy exhibits no sign of variation in rotation speed with radius over the whole radial range from 1 to 3 $R_{\rm eff}$. The reconstructed 2D velocity map of this galaxy is shown in Fig. 11.

Agreements with the σ profiles and PNe data in the literature are again good, with σ declining steadily with radius within 1 $R_{\rm eff}$, but levelling off beyond. Indeed, beyond 1 $R_{\rm eff}$, the data are consistent with *no* slope in σ at the 1σ confidence level.

The kinematic PA exhibits a shift of ∼10° at ∼1.5 $R_{\rm eff}$, mirroring the shift in photometric PA (Napolitano et al. 2009).

The rotation axis ratio is similar to the photometric axis ratio in the innermost regions, but falls rapidly at the radius at which the PA changes. The photometric axis ratio (Napolitano et al. 2009), on the other hand, remains near constant with radius. The disparity in axis ratios is all the more curious when the lack of photometric evidence for an embedded disc at these radii (Carollo et al. 1997) is considered. However, it is interesting to note that the kinematic axis ratio in the outer regions of the galaxy is similar to the photometric axis ratio of the central embedded disc of ∼0.5 (Carollo et al. 1997). This suggests that the inner disc could in fact be part of a much larger (warped) disc structure.

The interpretation of the kinematics in this galaxy is clearly complex. The highly elliptical $V_{\rm rot}$ and h_3 at ∼1 $R_{\rm eff}$ and their possible association with the central disc would seem to suggest that this galaxy harbours an embedded stellar disc at large radii. However,

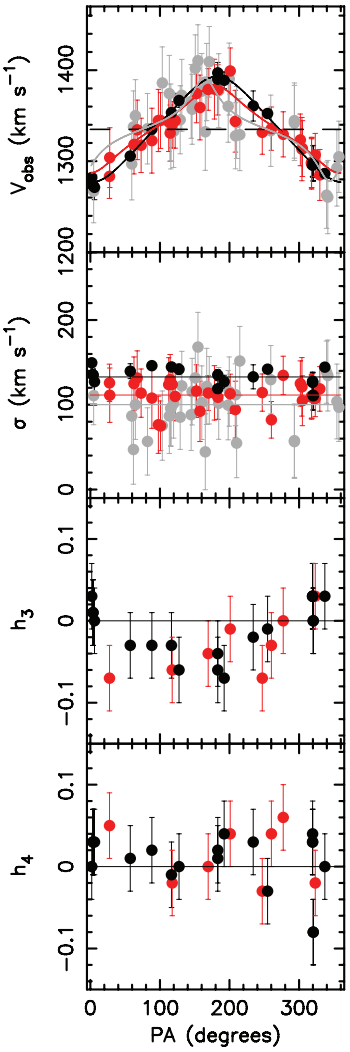

Figure 9. *NGC 4494*. Same as Fig. 6. The major axis PA is 173°.

the lack of photometric evidence for such a disc raises serious questions about such an interpretation. An alternative description is suggested by the results of Balcells (1991) who shows that the signature of rotation accompanied by an h_3 signal can be generated by a minor merger event, as a result of the redistribution of the angular momentum of the merging galaxy. Such an event could also be responsible for the shift in photometric and kinematic PAs at ∼1.5 $R_{\rm eff}$. Our results are therefore at least qualitatively consistent with the idea that this galaxy is a merger remnant. The presence of a kinematically distinct core (Bender 1988) also supports this interpretation.

4.3 NGC 1407

NGC 1407 is the brightest group galaxy in a dwarf-galaxy-dominated group (Trentham, Tully & Mahdavi 2006). The galaxy has been classified as a weakly rotating E0 (Longo et al. 1994) with a 'core like' central luminosity profile (Lauer et al. 1995; Spolaor et al. 2008a). The stellar population analysis of Spolaor et al. (2008b) found the galaxy to possess a uniformly old age within ∼0.6 $R_{\rm eff}$.

Plots of velocity moments with PA are presented in Fig. 12. The data were not fitted for kinematic axis ratio due to low signal-to-

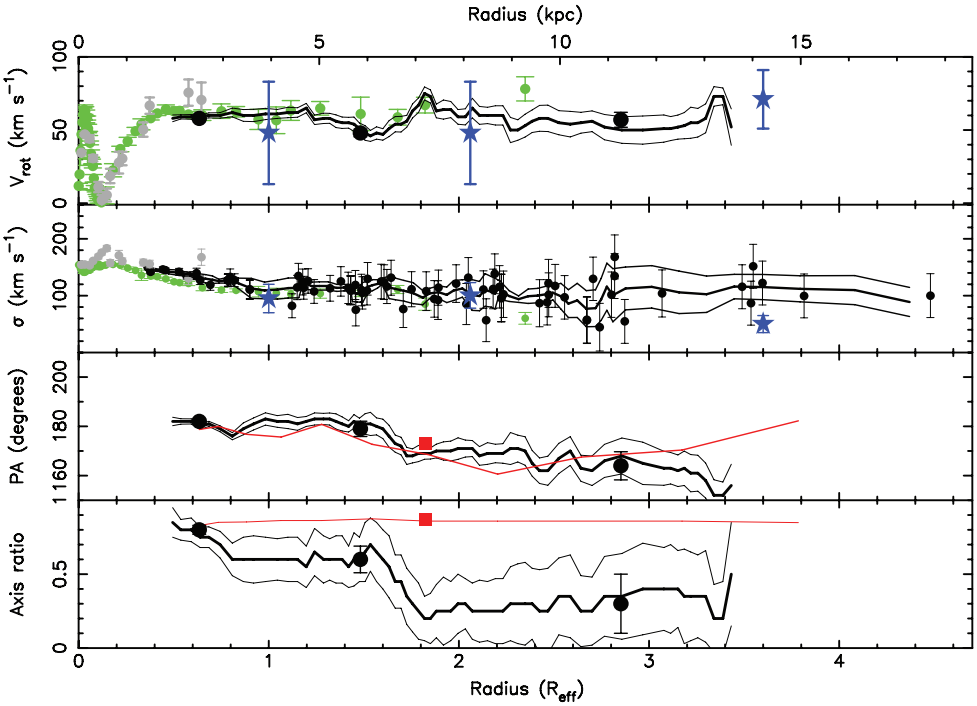

Figure 10. *NGC 4494*. Same as Fig. 7 with the following exceptions. Green data points in V_{rot} and σ plots are the major axis data from Napolitano et al. (2009). The PN data (blue stars) are also from Napolitano et al. (2009). Grey data points are the data of Bender, Saglia & Gerhard (1994). Red lines in plots of PA and axis ratio are the V-band results of Napolitano et al. (2009). Large offsets between the kinematic and photometric axis ratio and PAs can be seen.

noise ratio and the large uncertainties in fits of axis ratio when the value approaches 1.0. However, it is clear from the plot of V_{obs} with PA that the rotation has very low ellipticity (kinematic axis ratio ∼1.0), similar to the 2MASS photometric axis ratio of 0.95. This value was therefore assumed for the rolling fits. A slow (∼25 km s^{-1}) rotation is evident in all three radial bins. There is a suggestion of non-zero h_3 in the inner regions, consistent with the results of the re-analysis of Spolaor et al. (2008a) data (see Appendix A). The data suggest a declining σ with radius.

Rolling fits were performed on the V_{obs} data using 12 data points in the inner region rising to 20 data points in the outer regions of the galaxy (Fig. 13). The results confirm the near constant V_{rot} with radius between ∼0.5 and 3 R_{eff} (we note that the variations with radius are only of order 1σ significance). Fig. 13 also confirms the shallow decline in σ with radius identified above. The reconstructed 2D velocity map of this galaxy is shown in Fig. 11.

PA_{kin} shows a ∼2σ deviation from the photometric PA of Goudfrooij et al. (1994) in the inner regions ($\lesssim$1.0 R_{eff}), but is in good agreement with the 2MASS photometric PA at 1.5 R_{eff}. The cause of the apparent discrepancy in the inner regions is unclear, although significant triaxiality is one possible cause. However, it may also simply be the result of the large uncertainties that arise when fitting both photometric and kinematic data when axis ratios approach unity.

4.4 NGC 1400

Variously classified as an E (e.g. Da Costa et al. 1998) and an S0 (e.g. 2MASS; Jarrett et al. 2003), this galaxy is associated, but apparently not interacting with, the NGC 1407 group. Spolaor et al. (2008b) found the stellar population to possess a uniformly old age out to ∼1.3 R_{eff}.

The distribution of V_{obs} and σ with PA is shown in Fig. 14. As for NGC 1407, the kinematic axis ratio was not fitted. Instead, the 2MASS photometric axis ratio of 0.9 was assumed. For this galaxy, the signal-to-noise ratio was too low for the accurate measurement of the h_3 and h_4 moments. These were therefore suppressed during kinematic analysis using the pPXF code (Section 3). However, we note the significant h_3 detection in the re-analysis of the Spolaor et al. (2008a) data (Appendix A). Our data sampled only one data point within 1 R_{eff}. Radial binning was therefore carried out in the bins $R < 1.5\ R_{eff}$ and $R \geq 1.5\ R_{eff}$. For some of the outermost points errors in velocity dispersion exceeded 100 km s^{-1}. These data were omitted from both plots and analysis.

Fig. 14 shows that V_{rot} is lower in the outer radial range than in the inner range. There is also the suggestion of a falling σ with radius. The data were not fitted for rotation axis ratio due to low signal-to-noise ratio and the large uncertainties in fits in axis ratio measurements when the value approaches 1.0. However, it is clear from the plot of V_{obs} with PA that the rotation has very low ellipticity (rotation axis ratio ∼1.0), similar to the 2MASS photometric axis ratio of 0.90. This value was therefore assumed for the rolling fits.

Because of the small sample size, rolling fits were performed to V_{obs} using seven points in the inner region rising to 12 in the outer regions. The resultant plots with radius (Fig. 15) confirm the conclusions drawn from the plot with PA of a falling V_{rot} and σ with radius. Indeed, this galaxy shows the sharpest fall-off in σ with radius in our sample – falling from >300 km s^{-1} in the centre to ∼100 km s^{-1} at ∼1.5 R_{eff}, but remaining near constant beyond. However, there appears to be a significant unexplained offset between σ from this work and the values from the data of Spolaor et al. (2008a) in the overlap region (both before *and* after the re-measurement of the data using the pPXF; see Appendix A). It is important to note that this discrepancy increases with decreasing radius, with the discrepancy rising from ∼20 km s^{-1} at 1.4 R_{eff} to

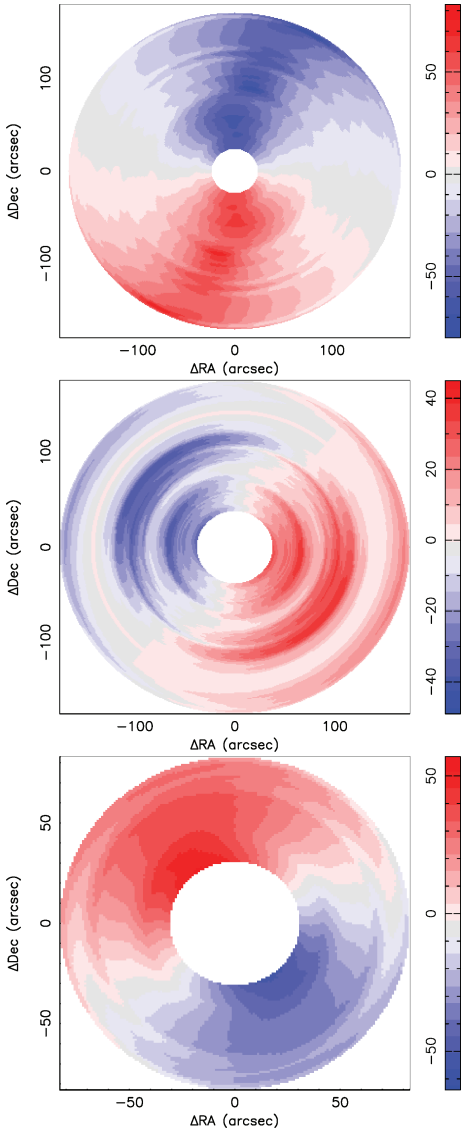

Figure 11. Reconstructed 2D velocity maps of (top to bottom) NGC 4494, NGC 1407 and NGC 1400. Colour scales (in km s^{-1}) are shown to the right of each image. Note that the variations in $V_{\rm rot}$ with radius in NGC 1407 that causes the unusual patterning in the reconstruction are only detected at $\sim$1σ significance.

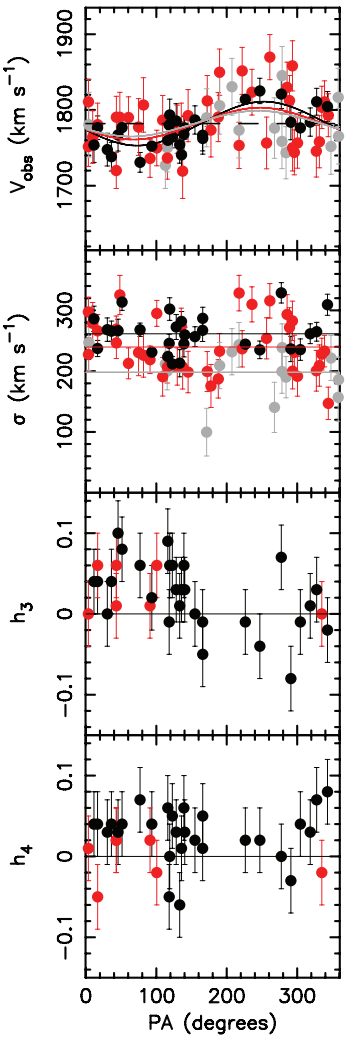

Figure 12. *NGC 1407*. Same as Fig. 6 except that the rotation axis ratio was not fitted but assumed to be equal to the 2MASS photometric axis ratio (i.e. 0.95). The major axis PA is 60°.

60 km s^{-1} at 1 $R_{\rm eff}$ (see also Fig. 5). This clearly indicates that this is not a signal-to-noise ratio issue. A detailed examination of the spectra of the two studies of NGC 1400 could identify no obvious reasons for such a discrepancy. Consequently, we must contemplate the possibility that this is a real effect. We therefore note that the sense of the discrepancy is consistent with the idea that the optical and near-infrared (NIR) probe different stellar populations, with the NIR being dominated by a lower velocity dispersion (more centrally concentrated) population than the optical. The strong stellar population metallicity gradient in NGC 1400 (−0.38 dex/dex; Spolaor et al. 2008b) may therefore be the cause of the large discrepancy in this galaxy. The reconstructed 2D velocity map of this galaxy is shown in Fig. 11.

$PA_{\rm kin}$ shows no significant variation with radius and is in good agreement with the photometric PA of 2MASS and Spitler et al. (in preparation).

With regard to this galaxy's rather uncertain morphological classification, the evidence for a disc with a declining rotation, but near constant σ profile would seem to favour its classification as an elliptical with an embedded disc.

4.5 NGC 821

NGC 821 is an isolated (Reda et al. 2007), elliptical galaxy with morphological classification E6. The galaxy is considered to possess a disc embedded in an spheroidal halo (Michard & Marchal 1994; Ravindranath, Ho & Filippenko 2002; Emsellem et al. 2004). The photometric profiles of Goudfrooij et al. (1994) show that ellipticity peaks around 15 arcsec ($\sim$0.3 $R_{\rm eff}$). Kinematic profiles have been widely published (e.g. Pinkney et al. 2003; Proctor et al. 2005; Forestell & Gebhardt 2008), although there is still some debate as to whether the σ profile is falling or not and whether NGC 821 contains dark matter (Romanowsky et al. 2003). The stellar population study of Proctor et al. (2005) reveals a young central stellar population which gives way to old ages by 1 $R_{\rm eff}$.

Plots of velocity moments with PA are shown in Fig. 16. Only the data within 1 $R_{\rm eff}$ were fitted for PA and rotation axis ratio due to

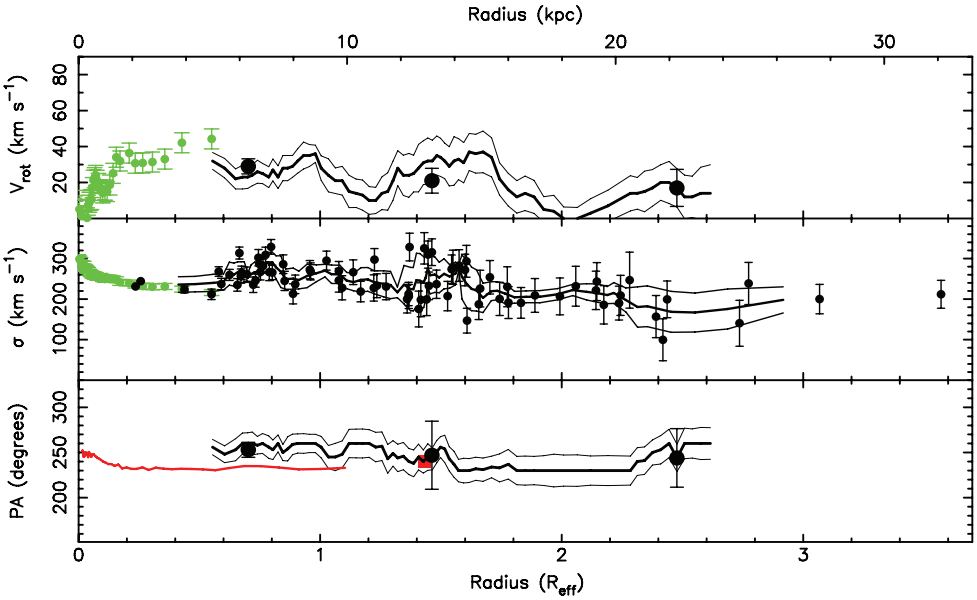

Figure 13. *NGC 1407*. Same as Fig. 6 with the following exceptions. Kinematic axis ratio is not presented as the proximity of the rotation axis ratio to 1.0 makes its constraint beyond the capabilities of the signal-to-noise ratio of our data. In the V_{rot} and σ plots green points are from our remeasurement of the data of Spolaor et al. (2008a) (see Appendix A). The red line in the PA plot is the *I*-band data of Goudfrooij et al. (1994). Photometric PAs are shown with a 180° offset for the purpose of comparison to the kinematic data.

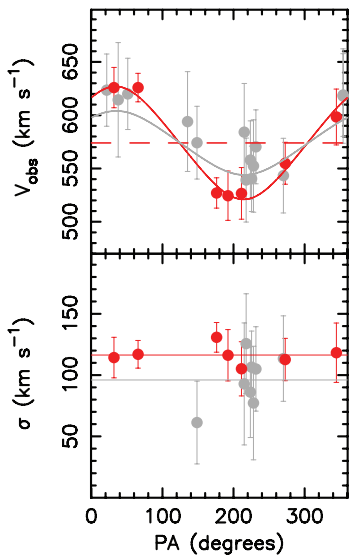

Figure 14. *NGC 1400*. Same as Fig. 6 with the following exceptions. The velocity moments h_3 and h_4 were suppressed in this low signal-to-noise ratio sample. Radial bins of the independent data points are $R < 1.5\,R_{\rm eff}$ and $R \geq 1.5\,R_{\rm eff}$. The rotation axis ratio was not fitted but assumed to be 0.9 (i.e. equal to the 2MASS photometric axis ratio).

low signal-to-noise ratio and small sample size in the outer regions. The values derived from the inner regions were then assumed for the outer regions.

Fig. 16 shows strong rotation within $1\,R_{\rm eff}$, but exhibits a value consistent with zero rotation beyond this region. We also detect no variation in σ with radius.

Rolling fits of the rotation velocity data (Fig. 17) were performed using seven data points in the inner region rising to 12 data points in the outer regions of the galaxy. Fig. 17 confirms the falling V_{rot} with radius and flat σ identified in the plots with PA. The figure also shows that, where they overlap, there is good agreement between our results and both the Emsellem et al. (2004) and Forestell & Gebhardt (2008) results for V_{rot}, σ, PA_{kin} and kinematic axis ratio, although we note one discrepant data point of Forestell & Gebhardt at $1.8\,R_{\rm eff}$.

Our σ values are also in good agreement with literature studies of both stellar and PNe kinematics. We note that Coccato et al. (2009) also measure a PN rotation velocity consistent with zero for a data point at $5\,R_{\rm eff}$ with rotation and σ of 14 ± 25 and $51 \pm 18\,{\rm km\,s^{-1}}$, respectively.

The single kinematic axis ratio value that we derive is significantly lower than the photometric axis ratio, confirming the result found using the SAURON data (Krajnović et al. 2008).

It is also interesting to note that the extent of the disc evident in the V_{rot} plot of Fig. 17 is similar to the extent of both the dip in photometric axis ratio of Goudfrooij et al. (1994) (bottom plot, Fig. 17) *and* to the extent of the young central population identified in Proctor et al. (2005), both of which are evident out to nearly $1\,R_{\rm eff}$. This lends credence to the speculation that the young central ages are associated with the presence of a disc that has undergone a recent burst of star formation. Also of interest is the fact that the photometric axis ratio of the galaxy remains fairly low (∼0.7) even at radii well beyond the extent of the disc. This suggests that the galaxy is composed of a disc embedded in a highly elliptical bulge in agreement with the photometric classification in the literature (Michard & Marchal 1994; Ravindranath et al. 2002; Emsellem et al. 2004).

To aid in the visualization of our results, and to facilitate the comparison of our results with those of SAURON (Emsellem et al. 2004), we have reconstructed the 2D rotation map of the galaxy in Fig. 18. The image was generated using the rolling fit values of V_{rot} of Fig. 17 and assuming rotation to have constant PA_{kin} and axis ratio, with values equal to the values within $1\,R_{\rm eff}$ (33° and 0.3,

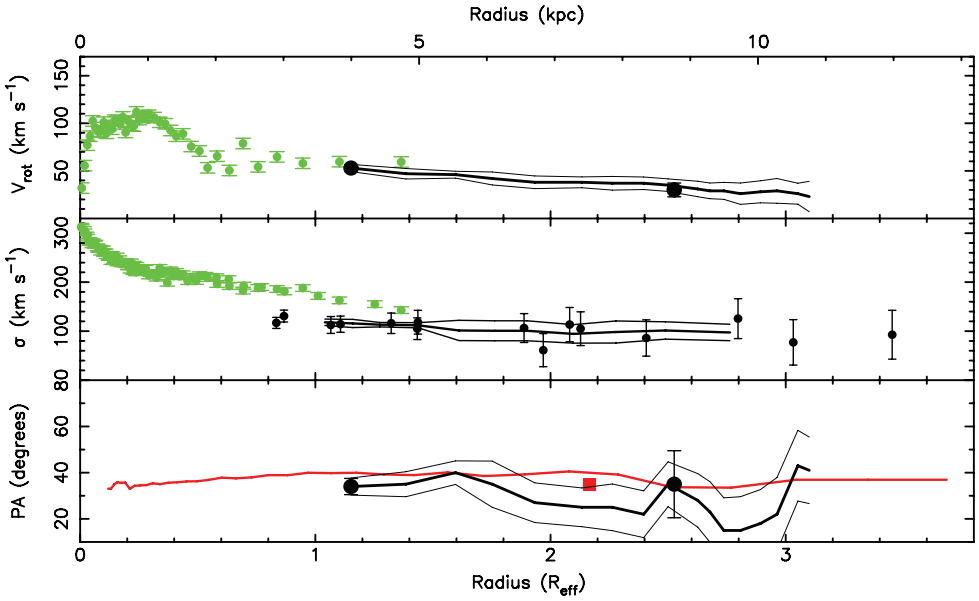

Figure 15. *NGC 1400*. Same as Fig. 7 with the following exceptions. The independent data points are for $R < 1.5\,R_{\rm eff}$ and $R \geq 1.5\,R_{\rm eff}$. Green data points in $V_{\rm rot}$ and σ plots are from the remeasurement of the data of Spolaor et al. (2008a) (see Appendix A). The red line in the PA plot is the Sloan *i*-band data of Spitler et al. (in preparation).

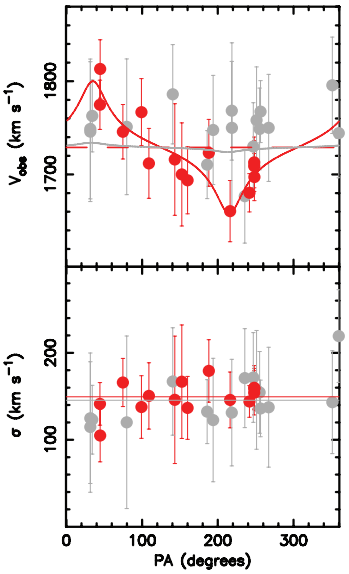

Figure 16. *NGC 821*. Same as Fig. 14 except that the radial binning is in ranges of $R < 1.0\,R_{\rm eff}$ and $R \geq 1.0\,R_{\rm eff}$ only. The major axis PA is 30°.

respectively; Table 4). The SAURON map is also shown. Despite the spatial gap between the two data sets, agreement can be seen to be good.

5 DISCUSSION

We have demonstrated that our analysis gives good agreement with the SAURON (Emsellem et al. 2004) study and other data from the literature in regions where they overlap. We have also shown that the results provide valuable insights into individual galaxies. We next consider our results in a more general sense.

5.1 Rotation

The five galaxies in our sample exhibit a range of rotation profiles. Two galaxies (NGC 1407 and NGC 4494) exhibit flat rotation profiles (within errors) beyond 0.2 and 0.4 $R_{\rm eff}$, respectively. One galaxy (NGC 2768) exhibits rotation that increases in amplitude over the full extent of our data (i.e. to $\sim$3 $R_{\rm eff}$). The remaining two galaxies (NGC 821 and NGC 1400) exhibit rotation curves that decline beyond 1 $R_{\rm eff}$, and in the case of NGC 821, becomes consistent with zero rotation by 1.5 $R_{\rm eff}$. It is therefore evident from our data that studies confined to the central regions of galaxies can miss vital aspects of their rotation properties.

5.2 Velocity dispersion

The five galaxies in our sample exhibit only shallow slopes in σ with radius beyond 1 $R_{\rm eff}$. Indeed, in most cases, results in these regions are consistent with zero slope at the 2σ significance level. Such flat σ and rotation profiles (with the possible exception of NGC 821) represent the classic signature of a dark matter halo in each galaxy. These data will therefore prove invaluable to future studies that perform full dynamical modelling of galaxies.

5.3 Higher order moments

We note that all five galaxies in this study exhibit non-zero h_3 values, the sense of which mirror the rotation velocity. This trend is identified in the NIR spectra of this work in three of the five galaxies. In NGC 1400 it is identified in the re-analysis of the Spolaor et al. (2008a) optical data, while in NGC 821 it is evident in the optical data of Forestell & Gebhardt (2008). When h_3 follows the inverse trend of the rotation velocity it is often taken as the signature of a cold (rotating) stellar population embedded within a hotter

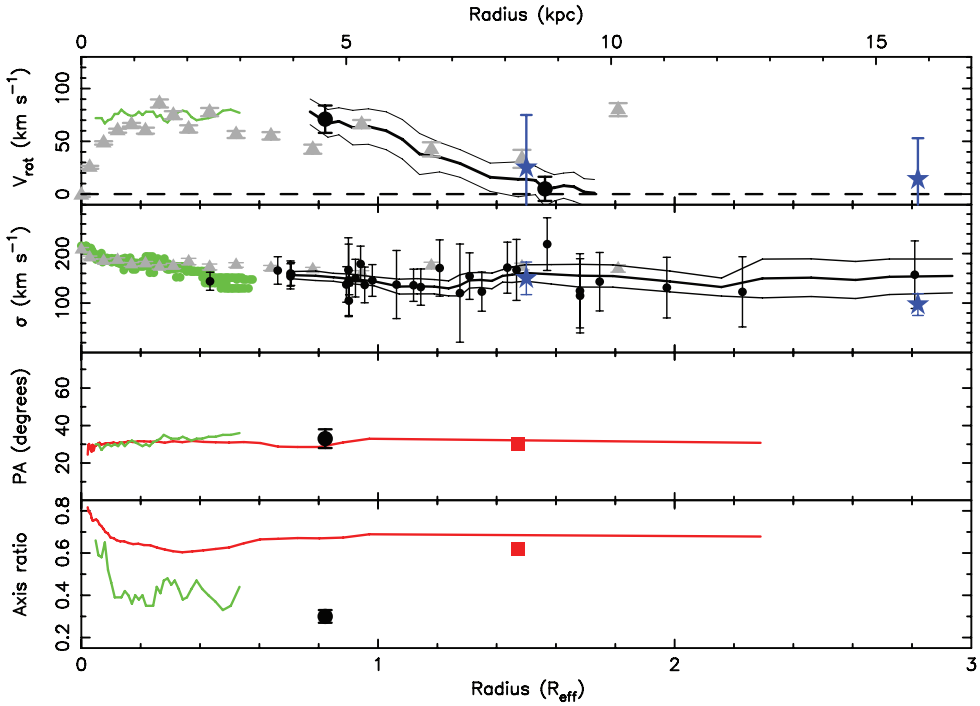

Figure 17. *NGC 821*. Same as Fig. 7 with the following exceptions. Radial binning is in ranges of $R < 1.0\,R_{\rm eff}$ and $R \geq 1.0\,R_{\rm eff}$ only. Kinematic PA and axis ratio were only estimated for the inner range. Inner range values of these parameters were *assumed* for the measurement of $V_{\rm rot}$. Green data points are from SAURON (Emsellem et al. 2004). Grey data points are from Forestell & Gebhardt (2008). Blue stars are the PN data of Coccato et al. (2009). Red lines in PA and axis ratio plots are the photometric data of Goudfrooij et al. (1994).

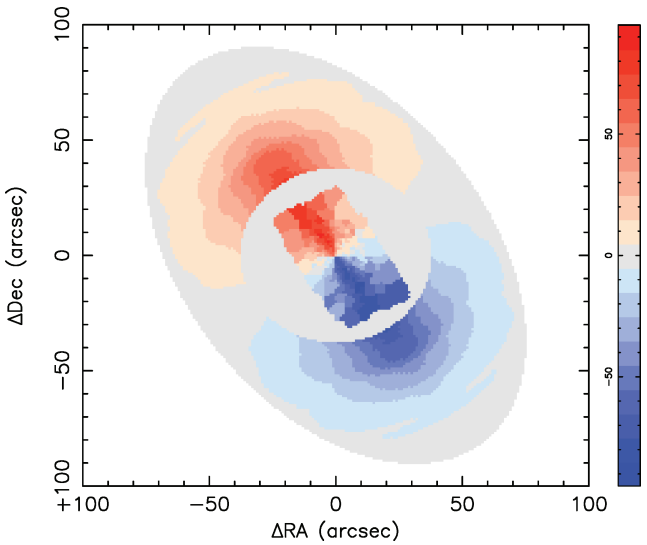

Figure 18. *NGC 821*. Reconstruction of the rotation profile using the rolling fits of $V_{\rm rot}$ (Fig. 17). However, beyond $1\,R_{\rm eff}$ the values of kinematic PA and axis ratio are *assumed* to be the same as within $1\,R_{\rm eff}$ (33° and 0.3, respectively). The outer boundary of the map has been chosen to reflect the photometric axis ratio of the galaxy (0.62). The colour scale (in km s^{-1}) is shown on the right. Also shown is the SAURON (Emsellem et al. 2004) map of the central regions of the galaxy. The agreement between the data sets is again extremely good.

(pressure supported) system. However, Balcells (1991) shows that this signature can also be induced by the action of a merger event. We therefore conclude that all five of the observed galaxies are either merger remnants or harbour embedded discs.

There do not appear to be any clear trends in the h_4 parameter in our current data. we suspect that this is due to the low signal-to-noise ratio of the majority of our data.

5.4 Kinematic and photometric misalignment

For fast rotators, the SAURON survey revealed that the kinematic and photometric PAs are usually well aligned, and that their axis ratios are similar (Emsellem et al. 2007). This is true for two of our galaxies (NGC 2768 and NGC 1400). However, in both NGC 4494 and NGC 821 there appear to be significant offsets between kinematic and photometric axis ratios, while for NGC 821 an offset in axis ratio is detected. This result for NGC 821 confirms the SAURON result, despite the fact that we have only one kinematic data point at large radii.

5.5 Anisotropy diagram

Binney (1978) showed the usefulness of the anisotropy diagram (V/σ versus photometric ellipticity) as applied to elliptical galaxies. In Fig. 19 we show this diagram for the two galaxies in common with the SAURON survey (i.e. NGC 821 and NGC 2768), with the lines indicating the radial variation. The plot shows that the value of V/σ in NGC 821 declines with increasing radius, while NGC 2768 increases. Thus NGC 821 trends away from the isotropic rotator line, while NGC 2768 trends towards it. It is therefore clear that the central regions of galaxies do not *necessarily* reflect the properties of galaxies as a whole, and care must be taken when drawing conclusions from central data only. We note that similar conclusions were reached from PN kinematics by Coccato et al. (2009).

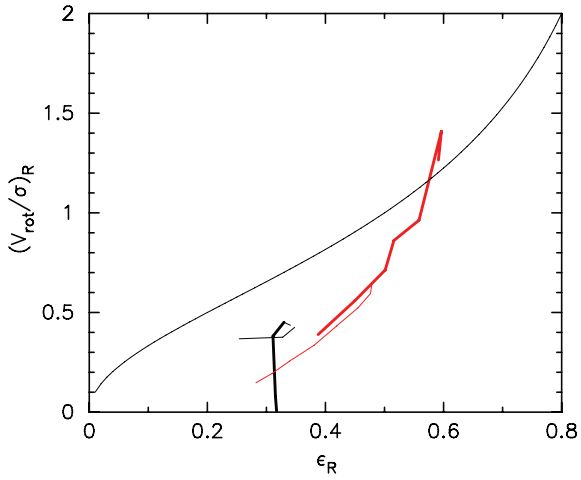

Figure 19. Anisotropy diagram. $V_{\rm rot}/\sigma$ is plotted against ellipticity at various radii for NGC 821 (black) and NGC 2768 (red). The remaining three galaxies are not shown as their $V_{\rm rot}/\sigma$ and photometric ellipticities show little or no variation with radius. The thin lines represent the inner SAURON data, and the thick lines are our data out to 3 $R_{\rm eff}$. The smooth curved line represents an ideal isotropic rotator.

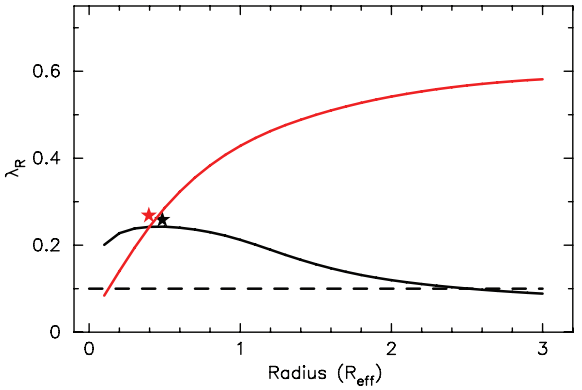

Figure 20. The λ_R parameter (cumulative value of λ within radius R) with major axis radius scaled by the $R_{\rm eff}$. The SAURON central values are presented as stars, and our data by solid lines. Here NGC 821 is black and NGC 2768 is red. The dashed line represents the delimiting value of 0.1 between 'fast' and 'slow' rotators (as defined in Emsellem et al. 2007). While both galaxies are classified as fast rotators based on SAURON data within 1 $R_{\rm eff}$, NGC 821 would be classified as a slow rotator if the data to 3 $R_{\rm eff}$ are considered.

5.6 The SAURON λ_R parameter

As part of the analysis of the SAURON 2D kinematics, Emsellem et al. (2007) defined a new parameter, λ_R, as

$$\lambda_R = \frac{\langle R|V|\rangle}{\langle R\sqrt{(V^2+\sigma^2)}\rangle}, \quad (3)$$

where $\langle R|V|\rangle$ is the luminosity weighted average of the product of radius and rotation velocity over the surface of the map and $\langle R\sqrt{(V^2+\sigma^2)}\rangle$ is a similar luminosity weighted average. Thus λ_R is a measure of the projected angular momentum per unit mass (i.e. the *specific* angular momentum).

Emsellem et al. (2007) found that galaxies were clearly distinguished into two classes on the basis of this parameter, i.e. 'fast rotators' ($\lambda_R > 0.1$) and 'slow rotators' ($\lambda_R < 0.1$). Fast rotators tended to be lower luminosity, discy ellipticals, while the massive boxy ellipticals were often slow rotators.

The two galaxies in common with the SAURON project (NGC 821 and NGC 2768) were both classified as 'fast rotators' (i.e. $\lambda_R > 0.1$) by Emsellem et al. (2007). Their λ_R values are very similar (0.258 and 0.268, respectively). However, we find that when probed to radii greater than 1 $R_{\rm eff}$ NGC 821 reveals a declining rotation velocity (and roughly constant velocity dispersion) profile. This suggests that if the outer region data were included the calculated λ_R value would be smaller. Although due to the luminosity weighting in the λ_R definition more emphasis is given to the central regions, so the actual change in the value might be small.

To test this, we constructed a model of each of these galaxies. Each model assumed $R^{1/4}$ de Vaucouleur's (1953) profiles. For each galaxy, the rotation parameters ($V_{\rm rot}$, $\rm PA_{kin}$ and kinematic axis ratio) were then characterized by a polynomial fit to the plots with radius (Figs 7 and 17). The luminosity and velocity maps so produced were then combined as per Emsellem et al. (2007) to calculate the λ_R values inside ellipses of increasing $R_{\rm eff}$.[2] The results are presented in Fig. 20. Agreement with the published SAURON values for the inner regions can be seen to be extremely good. However, for NGC 821 our model suggests that, despite its classification as a fast rotator (when only data from within 1 $R_{\rm eff}$ is considered), the decreasing rotation at large radii could indeed result in the galaxy being classified as a slow rotator when all the data out to 3 $R_{\rm eff}$ are considered.

In contrast to NGC 821, NGC 2768 has a profile that continues to rise all the way out to $\sim$3 $R_{\rm eff}$. Its λ_R value will therefore continue to increase as larger and larger radii are included in the calculation, and the galaxy will remain a 'fast rotator'. Therefore, despite their similarity within 1 $R_{\rm eff}$, both of these galaxies have vastly different distributions of angular momentum with radius (see also Coccato et al. 2009).

Although not observed in the SAURON survey, we assume NGC 1407 to be a slow rotator, as its V/σ value is low (we estimate 0.09 on the basis of equation 23 of Cappellari et al. 2007) and its kinematics are similar to NGC 5982 which was observed by SAURON (Krajnović et al. 2008) and defined as a slow rotator (Emsellem et al. 2007). In the case of NGC 1400 and NGC 4494 their relatively high rotation velocities and relatively low velocity dispersions clearly indicate them to be fast rotators.

5.7 The rms velocity parameter

In addition to the $V_{\rm rot}/\sigma$ and λ_R parameters which probe orbital anisotropy and angular momentum, respectively, another fundamental parameter of a galaxy is its internal kinematic energy. The observational measure of the total kinetic energy is the rms velocity parameter, which *locally* is equal to the quadrature combination of rotation and dispersion velocities, i.e. $V_{\rm rms} = \sqrt{V_{\rm rot}^2+\sigma^2}$ (e.g. Napolitano et al. 2009).

In Fig. 21 we show the rms velocity parameter as a function of major axis radius for the five galaxies in our sample. We show the inner regions from literature data and the outer regions from our data. For all but one galaxy (NGC 2768) a general decline in the rms velocity parameter is seen with radius (as might be expected from the generally flat rotation velocity and declining velocity dispersion profiles observed). The implications of this for the mass profile of each galaxy require detailed dynamical modelling.

[2] Although precise values of the Sersic index for the two galaxies are not available, we note that the results are relatively insensitive to this parameter.

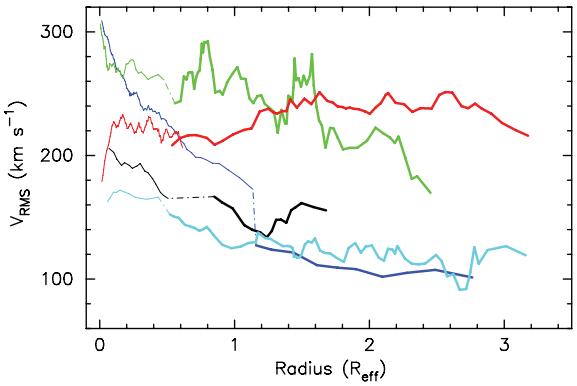

Figure 21. V_{rms} parameter with major axis radius. Galaxies are colour coded, i.e. NGC 821 black, NGC 1400 blue, NGC 1407 green, NGC 2768 red and NGC 4494 cyan. The thin lines represent the inner literature data, and the thick lines are our data out to larger radii (with extrapolated dashed lines connecting the two). In general the V_{rms} profiles decline with radius.

6 CONCLUSIONS

We have developed a new technique for extracting spectra of the galaxy background contained in the multi-object observations using the DEIMOS spectrograph on the Keck telescope. Here the slits contained GCs, which were the primary target of the observing programme. The technique allows measurement of the velocity moments (rotation velocity, velocity dispersion and Gauss–Hermite coefficients h_3 and h_4) in a galaxy halo out to at least $3\,R_{\rm eff}$, covering a surface area of some $24\,R_{\rm eff}^2$, in comparison to the $\sim$0.4 $R_{\rm eff}^2$ achieved by the SAURON IFU.

For the five early-type galaxies in our sample, we have demonstrated that the agreement between our results and the literature values is generally extremely good in the regions of overlap, including the velocity dispersion profiles from PNe data for NGC 821 and NGC 4494.

For NGC 821 we show that the kinematic signature of the disc identified in the surface photometry disappears at around $1.5\,R_{\rm eff}$, while the photometry remains highly elliptical in the outer regions. From this we conclude that NGC 821 constitutes a highly elliptical bulge with an embedded central disc. For NGC 1400, we also detect a falling rotation profile beyond $1\,R_{\rm eff}$. When considered in conjunction with the significant h_3 found by Spolaor et al. (2008a) in the inner regions, this suggests that this early-type galaxy also contains an embedded disc. For both NGC 1407 and NGC 4494, which are currently classified as pure elliptical galaxies, the detection of a trend in the Gauss–Hermite h_3 coefficient suggests that these too harbour a subpopulation with 'disc-like' kinematics. In NGC 4494, both the 'disc-like' kinematics *and* a coordinated shift in photometric and kinematic PAs provide strong support for the idea that this galaxy is a merger remnant. The kinematics of NGC 2768 clearly indicates that a disc is present. However, in this case, the disc becomes more prominent with galactocentric radius, suggest that this galaxy is, in fact, an S0. It is therefore apparent that all five galaxies in our sample show evidence for a disc or disc-like components.

We estimate the angular momentum parameter λ_R used in the SAURON survey to classify early-type galaxies as either fast or slow rotators. Importantly, our analysis shows that the central kinematics is not necessarily representative of the kinematics at larger radii, and that galaxies can change their rotator class when data from larger radii are considered. This has important repercussions for any attempts to classify galaxies by their central kinematic properties alone.

We have shown that our sample galaxies reveal the relatively flat rotation and velocity dispersion profiles suggestive of massive dark matter haloes, thus demonstrating the value that our new technique will have when full dynamical modelling of these galaxies is carried out.

Finally, we note that the observations used here were not optimized for this project. Future work that uses slit masks designed for the purpose of extracting galaxy halo spectra should provide additional improvements.

ACKNOWLEDGMENTS

The analysis pipeline used in this work to reduce the DEIMOS data was developed at UC Berkeley with support from NSF grant AST-0071048. We also use the excellent Penalized Pixel-Fitting method (pPXF) code developed by Cappellari & Emsellem (2004) and the data products from the 2MASS, which is a joint project of the University of Massachusetts and the Infrared Processing and Analysis Center/California Institute of Technology, funded by the National Aeronautics and Space Administration and the National Science Foundation. The authors acknowledge the data analysis facilities provided by IRAF, which is distributed by the National Optical Astronomy Observatories and operated by AURA, Inc., under cooperative agreement with the National Science Foundation. This work was supported by the National Science Foundation under grants AST-0507729 and AST-0808099. JS was supported by NASA through a Hubble fellowship, administered by the Space Telescope Science Institute, which is operated by the Association of Universities for Research in Astronomy, Incorporated, under NASA contract NAS5-26555. Finally, we also thank the Australian Research Council for funding that supported this work.

REFERENCES

Balcells M., 1991, A&A, 249, L9
Bender R., 1988, A&A, 193, L7
Bender R., 1990, A&A, 229, 441
Bender R., Saglia R. P., Gerhard O. E., 1994, MNRAS, 269, 785
Binney J., 1978, MNRAS, 183, 501
Cappellari M., Emsellem E., 2004, PASP, 116, 138
Cappellari M. et al., 2007, MNRAS, 379, 418
Carollo C. M., Franx M., Illingworth G. D., Forbes D. A., 1997, ApJ, 481, 710
Coccato L. et al., 2009, MNRAS, 394, 1249
Da Costa L. N. et al., 1998, AJ, 116, 1
Dekel A., Stoehr F., Mamon G. A., Cox T. J., Novak G. S., Primack J. R., 2005, Nat, 437, 707
Denicoló G., Terlevich R., Terlevich E., Forbes D. A., Terlevich A., 2005, MNRAS, 358, 813
de Vaucouleurs G., 1953, MNRAS, 113, 134
de Vaucouleurs G., de Vaucouleurs A., Corwin H. G., Buta R. J., Paturel G., Fouque P., 1991, Third Reference Catalogue of Bright Galaxies. Springer-Verlag, Berlin (RC3)
Emsellem E. et al., 2004, MNRAS, 352, 721
Emsellem E. et al., 2007, MNRAS, 379, 401
Filippenko A. V., Chornock R., 2000, Int. Astron. Union Circ., 7511, 2
Forbes D. A., Franx Ma., Illingworth G. D., Carollo C. M., 1996, ApJ, 467, 126
Forestell A., Gebhardt K., 2008, ApJ, submitted (arXiv:0803.3626)
Fried D. L., Illingworth G. D., 1994, AJ, 107, 992
Gerhard O. E., 1993, MNRAS, 265, 213
Goudfrooij P., Hansen L., Jørgensen H. E., Nørgaard-Nielsen H. U., de Jong T., van den Hoek L. B., 1994, A&AS, 104, 179
Graham A. W., Colless M. M., Busarello G., Zaggia S., Longo G., 1998, A&AS, 133, 325

Hakobyan A. A., Petrosian A. R., McLean B., Kunth D., Allen R. J., Turatto M., Barbon R., 2008, A&A, 488, 523
Howell J. H., 2005, AJ, 130, 2065
Jarrett T. H., Chester T., Cutri R., Schneider S., Skrutskie M., Huchra J. P., 2000, AJ, 119, 2498
Jarrett T. H., Chester T., Cutri R., Schneider S. E., Huchra J. P., 2003, AJ, 125, 525
Jensen J. B., Tonry J. L., Barris B. J., Thompson R. I., Liu M. C., Rieke M. J., Ajhar E. A., Blakeslee J. P., 2003, ApJ, 583, 712
Krajnović D., Cappellari M., de Zeeuw P. T., Copin Y., 2006, MNRAS, 366, 787
Krajnović D. et al., 2008, MNRAS, 390, 93
Kronawitter A., Saglia R. P., Gerhard O., Bender R., 2000, A&AS, 144, 53
Lauer T. R. et al., 1995, AJ, 110, 2622
Longo G., Zaggia S. R., Busarello G., Richter G., 1994, A&AS, 105, 433
McDermid R. M. et al., 2006, MNRAS, 373, 906
McMillan P. J., Athanassoula E., Dehnen W., 2007, MNRAS, 376, 1261
Mamon G. A., Lokas E. L., 2005, MNRAS, 363, 705
Martel A. R. et al., 2004, AJ, 128, 2758
Mehlert D., Saglia R. P., Bender R., Wegner G., 2000, A&AS, 141, 449
Michard R., Marchal J., 1994, A&AS, 105, 481
Napolitano N. R. et al., 2009, MNRAS, 393, 329
Norris M. A. et al., 2008, MNRAS, 385, 40
Peletier R. F., Davies R. L., Illingworth G. D., Davis L. E., Cawson M., 1990, AJ, 100, 1091
Pinkney J. et al., 2003, ApJ, 596, 903
Proctor R. N., Forbes D. A., Forestell A., Gebhardt K., 2005, MNRAS, 362, 857
Proctor R. N., Forbes D. A., Brodie J. P., Strader J., 2008, MNRAS, 385, 1709
Ravindranath S., Ho L. C., Filippenko A. V., 2002, ApJ, 566, 801
Reda F. M., Proctor R. N., Forbes D. A., Hau G. K. T., Larsen S. S., 2007, MNRAS, 377, 1772
Rix H.-W., White S. D. M., 1992, MNRAS, 254, 389
Romanowsky A. J., Douglas N. G., Arnaboldi M., Kuijken K., Merrifield M. R., Napolitano N. R., Capaccioli M., Freeman K. C., 2003, Sci, 301, 1696
Romanowsky A. J., Strader J., Spitler L., Johnson R., Brodie J. P., Forbes D. A., Ponman T., 2008, ApJ, in press (arXiv:0809.2088)
Saglia R. P. et al., 1993, ApJ, 403, 567
Sánchez-Blázquez P., Gorgas J., Cardiel N., 2006, A&A, 457, 823
Sandage A., Bedke J., 1994, The Carnegie Atlas of Galaxies. Carnegie Institution of Washington with the Flintridge Foundation, Washington, DC
Sandage A., Tammann G. A., van den Bergh S., 1981, J. R. Astron. Soc. Canada, 75, 267
Sil'Chenko O., 2006, ApJ, 641, 229
Simkin S. M., 1974, A&A, 31, 129
Spolaor M., Forbes D. A., Hau G. K. T., Proctor R. N., Brough S., 2008a, MNRAS, 385, 667
Spolaor M., Forbes D. A., Proctor R. N., Hau G. K. T., Brough S., 2008b, MNRAS, 385, 675
Statler T. S., Smecker-Hane T., 1999, AJ, 117, 839
Thomas J., Jesseit R., Naab T., Saglia R. P., Burkert A., Bender R., 2007, MNRAS, 381, 1672
Tonry J. L., Dressler A., Blakeslee J. P., Ajhar E. A., Fletcher A. B., Luppino G. A., Metzger M. R., Moore C. B., 2001, ApJ, 546, 681
Trentham N., Tully R. B., Mahdavi A., 2006, MNRAS, 369, 1375
van der Marel R. P., 1994, MNRAS, 270, 271
van der Marel R. P., Franx M., 1993, ApJ, 407, 525
Weil M. L., Hernquist L., 1996, ApJ, 460, 101

APPENDIX A: THE RE-ANALYSIS OF NGC 1400 AND NGC 1407 LONG-SLIT DATA

Spolaor et al. (2008a) used the van der Marel & Franx (1993) code to measure velocity moments in 68 and 82 apertures along the major axes for NGC 1407 and NGC 1400, respectively. The spectra had a signal-to-noise ration of $\geq$30 Å^{-1} at 5000 Å, and reached a radial extent of 0.56 $R_{\rm eff}$ ($\sim$4.11 kpc) for NGC 1407 and 1.30 $R_{\rm eff}$ ($\sim$3.58 kpc) for NGC 1400. Measurement of moments was then carried out using 17 template stars of spectral class F5 to K4. Briefly, the procedure identified the template that best fit the central regions (where the signal-to-noise ratio is highest) and applied this to all spatial slices. The drawback to this method is that the best-fitting template was found using only the very central regions and the existence of strong stellar population gradients (particularly metallicity) may require differing templates in the inner and outer regions.

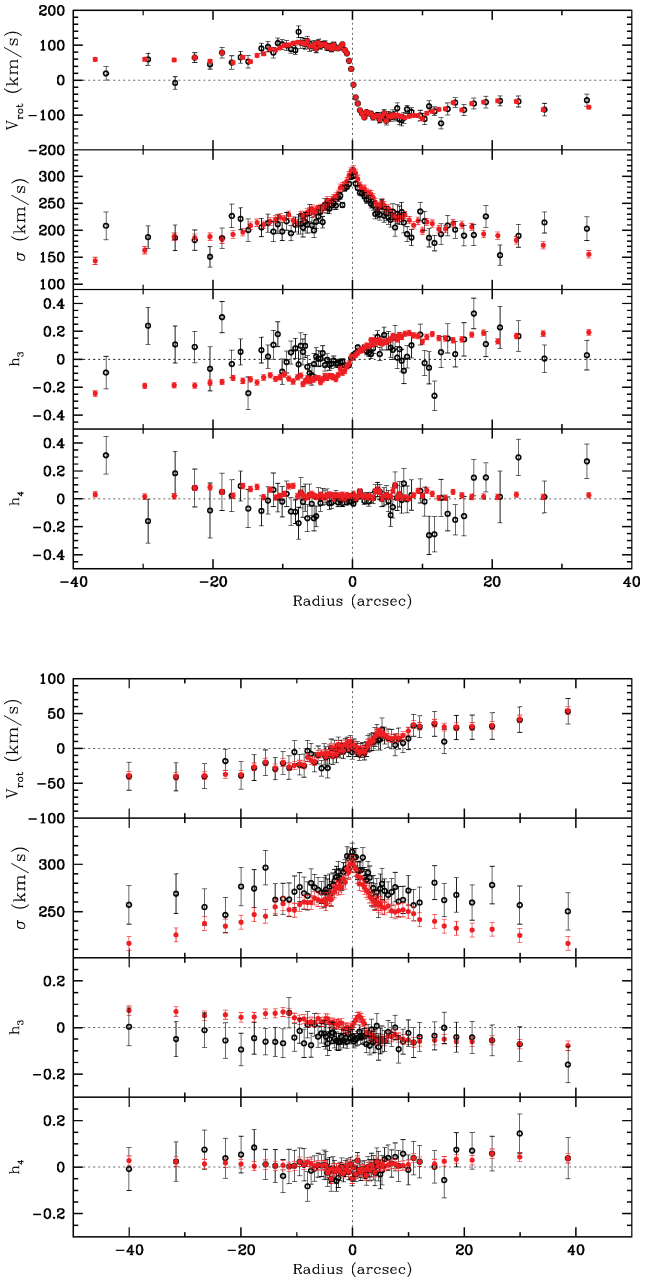

Figure A1. A comparison of the results of Spolaor et al. (2008a) (black points; NGC 1400, top and NGC 1407, bottom) to our re-analysis using the pPXF software (red points).

Table A1. New and old (Spolaor et al. 2008a) kinematic parameters for NGC 1400 and NGC 1407.

Parameter	New value	Old value
NGC 1400		
$V_{\rm sys}$	563 ± 5	560 ± 10
$V_{\rm rot}$	113 ± 6	139 ± 17
σ_0	281 ± 7	301 ± 4
NGC 1407		
$V_{\rm sys}$	1791 ± 5	1794 ± 10
$V_{\rm rot}$	54 ± 6	53 ± 19
σ_0	270 ± 7	313 ± 9

We have therefore re-analysed the data of Spolaor et al. (2008a) using the pPXF code of Cappellari et al. (2007). The main advantage of this code is following.

(i) A template match is found for *all* individual spatial slices.
(ii) The code finds the *combination* of templates that best matches the data, further improving the fit.

The results of the new fits are shown in Fig. A1 and Table A1. Errors on derived parameters were estimated by running a series of Monte Carlo simulations. The results do not change the general conclusions of Spolaor et al. (2008a). However, the kinematically decoupled core identified in Spolaor et al. (2008a) is now much more distinct and the h_3 and h_4 values appear much more consistent.

SUPPORTING INFORMATION

Additional Supporting Information may be found in the online version of this article.

Table 3. The velocity moment data from this work.

Please note: Wiley-Blackwell are not responsible for the content or functionality of any supporting material supplied by the authors. Any queries (other than missing material) should be directed to the corresponding author for the article.

This paper has been typeset from a TEX/LATEX file prepared by the author.